

PAPER • OPEN ACCESS

Global SOLPS-ITER and ERO2.0 coupling in a linear device for the study of plasma–wall interaction in helium plasma







To cite this article: G. Alberti *et al* 2023 *Nucl. Fusion* **63** 026020

View the [article online](#) for updates and enhancements.

You may also like

- [ERO2.0 modelling of the effects of surface roughness on molybdenum erosion and redeposition in the PSI-2 linear plasma device](#)
A Eksaeva, D Borodin, J Romazanov et al.
- [ERO2.0 modelling of nanoscale surface morphology evolution](#)
G. Alberti, M. Sala, J. Romazanov et al.
- [Plasma–surface interaction in the stellarator W7-X: conclusions drawn from operation with graphite plasma-facing components](#)
S. Breznsek, C.P. Dhard, M. Jakubowski et al.

Global SOLPS-ITER and ERO2.0 coupling in a linear device for the study of plasma–wall interaction in helium plasma

G. Alberti¹ , E. Tonello^{1,*} , P. Carminati¹, A. Uccello² , X. Bonnin³, J. Romazanov⁴ , S. Brezinsek⁴  and M. Passoni^{1,2} 

¹ Department of Energy, Politecnico di Milano, Milan 20133, Italy

² Istituto per la Scienza e Tecnologia dei Plasmi, CNR, Milan 20125, Italy

³ ITER Organization, 13067 St Paul Lez Durance Cedex, France

⁴ Forschungszentrum Jülich GmbH, Institut für Energie- und Klimaforschung–Plasmaphysik, Partner of the Trilateral Euregio Cluster(TEC), Jülich, Germany

E-mail: elena.tonello@polimi.it

Received 7 August 2022, revised 30 November 2022

Accepted for publication 19 December 2022

Published 3 January 2023



Abstract

Plasma–wall interaction (PWI) is a great challenge in the development of a nuclear fusion power plant. To investigate phenomena like erosion of plasma-facing components, impurity transport and redeposition, one needs reliable numerical tools for the description of both the plasma and the material evolution. The development of such tools is essential to guide the design and interpretation of experiments in present and future fusion devices. This contribution presents the first global simulation of PWI processes in a linear plasma device mimicking the boundary plasma conditions in toroidal ones, including both the description of plasma and impurity transport and of plasma-facing material evolution. This integrated description is obtained by coupling two of the state-of-the-art numerical codes employed to model the plasma boundary and the PWI, namely SOLPS-ITER and ERO2.0. Investigation of helium plasma is also of primary importance due to the role helium will have during ITER pre-fusion power operation, when it is planned to be used as one of the main plasma species, as well as fusion ash in full power operation. The plasma background is simulated by SOLPS-ITER and the set of atomic reactions for helium plasmas is updated, including charge-exchange and radiative heat losses. ERO2.0 is used to assess the surface erosion in the GyM vessel, using different wall materials (e.g. carbon, iron or tungsten) and applying different biasing voltage. Eroded particles are followed within the plasma to assess their redeposition location. The ionization probability of the different materials in the GyM plasma is inferred through the energy distribution of impacting particles and its effects on migration are investigated.

Keywords: linear plasma device, plasma–wall interaction, helium plasma, SOLPS-ITER, ERO2.0

(Some figures may appear in colour only in the online journal)

* Author to whom any correspondence should be addressed.



Original Content from this work may be used under the terms of the [Creative Commons Attribution 4.0 licence](https://creativecommons.org/licenses/by/4.0/). Any further distribution of this work must maintain attribution to the author(s) and the title of the work, journal citation and DOI.

1. Introduction

Plasma–wall interaction (PWI) is one of the main challenges in the path towards magnetically confined nuclear fusion [1]. Both plasma and materials can be severely affected by this interaction. Plasma-facing materials undergo erosion and surface modifications, which may limit components lifetime and alter their thermomechanical properties and, therefore, their power handling capabilities. Eroded impurities may enter the plasma core, thus diluting fuel and increasing radiation losses. The redeposition of these impurities, e.g. in the case of beryllium, is also one of the main contributors to tritium retention and dust formation, once redeposited layers become unstable [2].

Helium (He) plasmas play an important role with this respect, as He will be always present in the thermonuclear plasma of fusion devices and needs, as fusion product (ash), to be exhausted. Moreover, operation in He is foreseen for the pre-fusion power operation (PFPO) in ITER due to the expected lower H-mode power threshold with respect to hydrogen plasmas, opening to early application of Edge Localized Mode (ELM) mitigation schemes for safe and sustainable plasma operation [3]. In this framework, the prediction of PWI processes associated with He as fuel species and different plasma-facing materials in future devices is of fundamental importance. A combined approach of both experiment and modelling is essential to achieve this goal.

PWI experiments in existing tokamaks are of primary importance both in hydrogenic and He plasmas [4, 5]. This is testified by the extensive erosion studies performed in the recent campaign with hydrogen isotopes including T in JET [6] and by the interest for further investigation of He–W interaction with the recent He campaigns in JET-ILW and AUG in support of ITER. However, devices fully comparable to reactor relevant conditions are still not available, although the installation of the ITER-like wall in JET was a step in this direction. This points out the need for complementary devices which are able to reproduce the relevant features of the ITER plasma, in terms for example of particles and heat fluences onto the plasma-facing components (PFCs). Linear plasma devices (LPDs) have been routinely used to fulfill this purpose, investigating plasma detachment [7, 8] and showing the existence of a variety of plasma-induced surface modifications, primarily He-induced nanostructures, called tungsten (W) fuzz, that can form at the W plasma-facing surface under specific conditions [9–11]. Alongside with experimental efforts, the development of numerical codes is essential to better understand the underlying physics processes of the experimental results and to extrapolate them to conditions in future devices. Although LPDs can cover only a limited range of phenomena and conditions met in tokamaks, nonetheless their simple geometrical structure shall represent an attractive test-bed for the development and benchmarking of these numerical tools.

Two state-of-the-art codes for edge plasma and PWI modelling are SOLPS-ITER [12, 13], a 2D plasma fluid code already coupled with the neutral particle code EIRENE, and ERO2.0

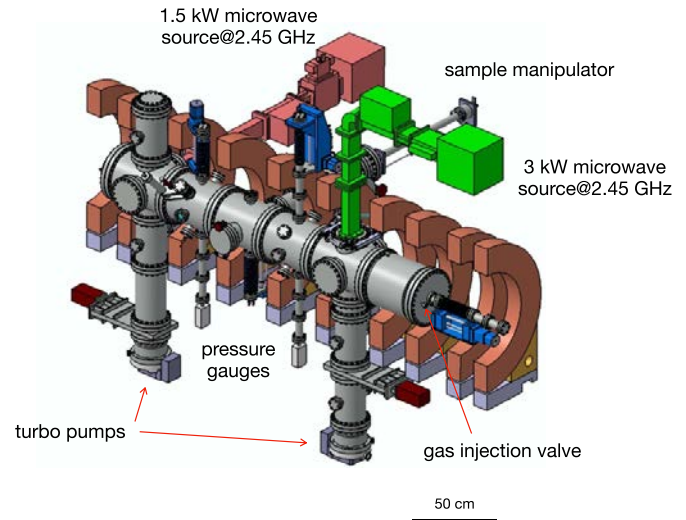


Figure 1. The GyM linear device of ISTP-CNR, Milano. The machine is made of ten magnetic coils, producing a maximum axial magnetic field of 0.13 T. The stainless steel vacuum chamber is approximately 2 m long and 0.25 m in diameter. Plasma is produced by two magnetron sources at 2.45 GHz. The gas injection is located on one of the two bases.

[14], a 3D Monte–Carlo code for impurity transport and PWI in trace approximation, respectively. During their development, different releases of both codes were separately applied to several LPDs [15–18]. In this work, we will consider the GyM linear device [19], which scheme is shown in figure 1. This machine operates at low magnetic field ($B \simeq 0.1$ T) and has plasma conditions similar to those of the scrape-off layer of toroidal devices. SOLPS-ITER has been recently used to simulate non-hydrogenic plasmas in GyM, like Ar [20] and He [21]. In both cases, the simulation results were benchmarked against experimental data, showing the capability of SOLPS-ITER of addressing the low temperature plasma conditions typical of linear devices. In [21], moreover, SOLPS-ITER results were also successfully compared with a simplified 0D model developed by space averaging of plasma main parameters. Erosion studies in GyM with ERO2.0 focused on the microscale surface morphology evolution of materials under plasma exposure [22]. Global erosion and migration using a suitable code for the plasma background were simulated with ERO2.0 in different tokamaks, such as JET [23], WEST [24] and ITER [25]. However, to the best of our knowledge, a similar study with the two codes has never been performed in LPDs.

This work presents an original modelling strategy to evaluate in an integrated manner the plasma background distribution and the erosion and redeposition of wall materials in linear plasma devices. Specifically, we performed the first global coupling between SOLPS-ITER and ERO2.0 in the GyM linear device, considering He plasma and different wall materials, such as carbon (C), iron (Fe), copper (Cu) and tungsten (W). From the results obtained in [21], we first added few collisional processes in the EIRENE input file that were neglected in previous SOLPS simulations of He plasmas. Once selected

the most complete atomic database for He simulations (see table 1), we simulated the GyM He plasma with SOLPS-ITER. This plasma background was then exploited for the ERO2.0 simulations, together with the 3D GyM internal geometry. The role of wall materials and of the application of a bias voltage on the wall (in the range from 0 to -200 V), thus controlling effectively the impact energy of the impinging plasmas species, is investigated. The coupling strategy and its main issues are addressed in section 2. Both SOLPS-ITER and ERO2.0 results are reported in section 3, while conclusions are drawn in section 4.

2. SOLPS-ITER and ERO2.0 coupling strategy

The SOLPS-ITER and ERO2.0 coupling scheme exploited in this work is shown in figure 2. The general idea is to use the distribution of the plasma inside the device, retrieved from densities, velocities and energies computed by SOLPS-ITER, and the magnetic equilibrium as input for the erosion calculations. Different *plasma backgrounds* are obtained by changing the inputs in SOLPS-ITER, e.g. including different atomic processes (see table 2), and their effects on the erosion properties can be assessed. The obtained plasma backgrounds are thus exploited by ERO2.0 to assess the particle and heat fluxes onto the PFCs, to compute erosion rates and to evaluate transport and redeposition of the eroded impurities. These phenomena are investigated varying the material of the PFCs and the energy of the impinging species, by applying a negative bias to part of the chamber wall.

ERO2.0 takes as input electron and ion quantities that are computed by the plasma solver of SOLPS-ITER, namely B2.5. This is a bi-dimensional multi-fluid code that solves Braginskii like equations [20, 26]. Rotational symmetry is assumed and the 2D computational mesh lies in the plane perpendicular to the symmetry direction: considering a cylindrical coordinate system (R, ϕ, z) , the B2.5 mesh lies in the (R, z) plane, as shown in figure 2(a).

ERO2.0, by contrast, is a 3D Monte–Carlo code and its computational domain covers the full cylindrical volume of the linear device. To provide the input for ERO2.0 the SOLPS-ITER quantities are interpolated on a full (R, ϕ, z) mesh, exploiting axial symmetry in the ϕ direction. While performing the interpolation of the plasma background from the computational grid of SOLPS—field-aligned in the (R, z) plane—to the (R, z) plane of the ERO grid—made of 2D rectangular cells—one has to consider two aspects: (a) the different space resolution and shape of the two meshes; (b) that the B2.5 mesh does not extend radially up to the wall, hence a proper extrapolation scheme should be used [23]. In the simulations we are considering in this work, a constant extrapolation of the last B2.5 radial value is used for all quantities since the outermost flux surface used to build the SOLPS-ITER mesh is just a few mm away from the lateral wall (figure 2(b)).

Finally, the 3D wall geometry of the GyM linear device is produced using a standard computer aided design (CAD) software (figure 2(c)). In this work we consider three main 3D

structures: (a) the two flanges at the base of the cylindrical chamber; (b) the lateral wall, including the holes present in the different sectors for the turbomolecular pumps, magnetron sources and the diagnostics; (c) 28 bushings, cylindrical structures (1 cm diameter, 2 cm height) protruding inside the plasma from the lateral wall, used for the positioning of a W liner inside the vacuum vessel made of steel. The sample holder is not modelled at this stage, to be consistent with the SOLPS-ITER plasma background. On top of these structures the polygonal mesh used by ERO2.0 to compute erosion and redeposition is built.

3. Results and discussion

3.1. SOLPS-ITER atomic database for helium plasmas

In this section, we discuss the results of SOLPS-ITER simulations, thus the plasma background for ERO2.0 ones. The main objective of the analysis presented here is the assessment of the effect of the atomic reactions considered in EIRENE (the Monte–Carlo neutral transport component within SOLPS-ITER) for a He plasma.

SOLPS is a tool widely used to investigate hydrogen and hydrogen-isotope plasmas. The associated database for atomic and molecular reactions is one of the richest in the context of edge plasma modelling. In most SOLPS applications, He, if present, is regarded as an impurity and, to avoid unnecessary complexities and reduce the computational cost of the simulations, only a limited number of reactions is considered. The SOLPS-ITER default set of reactions for He, thus, included only electron impact ionization (EI) and the effective⁵ recombination (RC) (reactions 1, 3, and 4 in table 1). Other processes, however, can become important if the concentration of He in the plasma increases and the impurity approximation is no longer valid. Understanding the impact of atomic processes on the overall plasma simulation and, if necessary, defining a more complete set of reactions for a He plasma play a key role in the upcoming modellings of pure He plasmas.

The reactions considered in this work are reported in table 1. In addition to default ones, electron impact excitation (reaction 2) in the electron energy balance, charge exchange (CX) reactions among helium ions and neutrals (reaction 5) and elastic collisions among He atoms (reaction 6) were included.

SOLPS-ITER simulations of the GyM linear device were performed using the setup described in [21]. In particular, the electron cyclotron resonance heating exploited in GyM was simulated with a Gaussian power density profile peaked at the axial position of the resonance, as explained in detail in [20]. A total absorbed power of $P_{\text{ext}} = 540$ W was considered. As concerns the neutral injection, a constant gas puff of $\text{Gas}_{\text{in}} = 9.0 \times 10^{18} \text{ He s}^{-1}$ was delivered. The particle anomalous diffusion coefficient was set to $D_n = 0.5 \text{ m}^2 \text{ s}^{-1}$ and the electron

⁵ Effective recombination, reaction 3 in table 1, includes radiative, dielectronic and three-body recombination. The energy recombination loss, reaction 4 in table 1, includes effective recombination and bremsstrahlung.

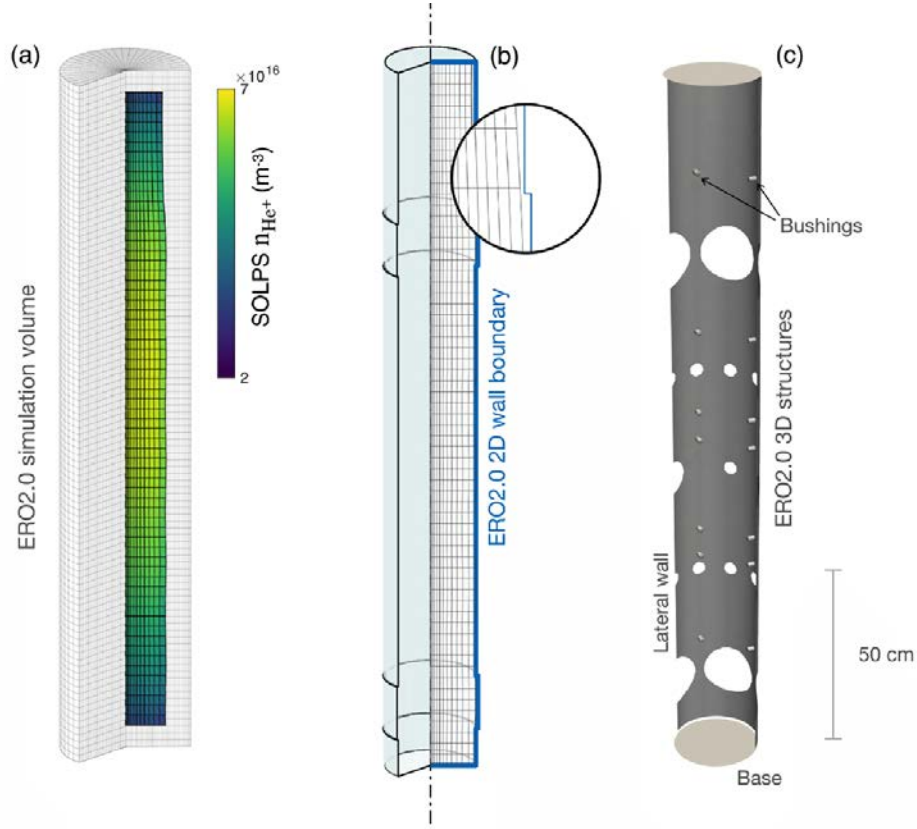


Figure 2. SOLPS-ITER and ERO2.0 global coupling scheme: (a) SOLPS-ITER plasma is projected onto 3D ERO2.0 grid. (b) Definition of 3D domain boundary for ERO2.0 simulation, by rotation of a 2D wall contour. (c) 3D CAD structures used by ERO2.0 to compute erosion and redeposition.

Table 1. Atomic reactions considered in the present work. For a detailed explanation of the reaction type refer to Eirene manual (www.eirene.de/). This is now the default set of reactions defined when helium is present among the plasma species, starting from SOLPS-ITER v. 3.0.8.

	Reaction	Type	Database
(1a)	$\text{He} + e^- \rightarrow \text{He}^+ + 2e^-$	EI-H.4	ADAS adf11/scd96
(1b)	$\text{He}^+ + e^- \rightarrow \text{He}^{2+} + 2e^-$		
(2a)	$\text{He} + e^- \rightarrow \text{He}^{(*)} + e^-$	EI-H.10	ADAS adf11/plt96
(2b)	$\text{He}^+ + e^- \rightarrow \text{He}^{+(*)} + e^-$		
(3a)	$\text{He}^+ + e^- \rightarrow \text{He}$	RC-H.4	ADAS adf11/acd96
(3b)	$\text{He}^{2+} + e^- \rightarrow \text{He}^+$		
(4a)	$\text{He}^+ + e^- \rightarrow \text{He} + h\nu$	RC-H.10	ADAS adf11/prb96
(4b)	$\text{He}^{2+} + e^- \rightarrow \text{He}^+ + h\nu$		
(5a)	$\text{He}^+ + \text{He} \rightarrow \text{He} + \text{He}^+$	CX-H.1-H.3	HYDHEL 5.3.1
(5b)	$\text{He}^{2+} + \text{He} \rightarrow \text{He} + \text{He}^{2+}$	CX-H.1-H.3	HYDHEL 6.3.1
(6)	$\text{He} + \text{He} \rightarrow \text{He} + \text{He}$	EL-H.2	AMMONX R-HE-HE

and ion thermal diffusivities were $\chi_{e,i} = 1.5 \text{ m}^2 \text{ s}^{-1}$. The results, in terms of the average electron density and temperature, are summarized in table 2.

Including electron impact excitation process in the electron energy balance equation, the power lost by electrons in interactions with neutral He per unit volume is computed as

$$P_{e,\text{He}}^{\text{loss}} = (E_{iz} \langle \sigma v \rangle_{iz} + \langle E \sigma v \rangle_{\text{PLT}}) n_e n_{\text{He}} \quad (1)$$

where E_{iz} is the He ionization energy, $\langle \sigma v \rangle_{iz}$ is the ionization rate coefficient and $\langle E \sigma v \rangle_{\text{PLT}}$ is the excitation energy rate coefficient [27]. Both rate coefficients are taken from ADAS (<https://open.adas.ac.uk>). An additional energy loss mechanism is introduced, besides ionization. However, unlike the ionization, electron impact excitation does not contribute to the creation of additional electrons. The fraction of external power used to create electrons is thus reduced leading to an overall density decrease. An analogous expression

Table 2. Volume average of plasma parameters (electron temperature T_e and electron density n_e) computed by SOLPS-ITER, including (✓) or neglecting (×) electron impact excitation heat loss (EI–ADAS/plt) and charge exchange (CX) reactions in EIRENE databases.

No.	EI (ADAS/plt)	CX	\bar{T}_e (eV)	\bar{n}_e (m ⁻³)
(1)	×	×	7.37	7.28×10^{16}
(2)	✓	×	7.35	5.65×10^{16}
(3)	✓	✓	6.89	10.66×10^{16}

exists for the power lost by electrons interacting with He⁺ ions, P_{e,He^+}^{loss} , although, due to the low ionization degree of GyM plasma, the dominant contribution here is $P_{e,He}^{\text{loss}}$. In this study, we used unresolved ADAS data [27], i.e. we considered the excited He meta-stable states to be in static equilibrium with the ground-state. A meta-stable resolved analysis could be of interest, especially in the low temperature plasmas of LPDs, and it is intended for future studies.

Including charge exchange reactions, collisional drag among ions and neutrals is activated. The effect is to increase the ion-to-wall confinement time, leading to an increase of the ion densities and a decrease in the electron temperature. This is shown in figure 3, where the 2D density distributions of He⁺, He²⁺ and He are shown for simulations without and including CX reactions. It can be noted that after including CX the neutral atom density decreases due to the increase of the ionization degree. These results agree with the findings presented in [21] that were obtained with a simplified 0D model. The same result is also presented in figure 4, where the radial (left) and axial (right) profiles of electron density and temperature are shown for simulations without (dotted) and with (solid) CX reactions.

The effect of He elastic collisions is very small ($\lesssim 2\%$) and it will not be considered in more detail.

3.2. Global erosion

He plasma background produced with SOLPS-ITER including all the reactions in table 1 is adopted for ERO2.0 simulations. The scheme described in section 2 is exploited for the coupling. ERO2.0 results concerning global erosion of GyM PFCs are summarized in this section, considering different wall materials.

As previously stated, ERO2.0 is a 3D Monte–Carlo code that is able to simulate plasma erosion of exposed materials and their subsequent migration within the volume of the considered device. Erosion is evaluated through pre-calculated sputtering yields, taking into account energy and angle of impinging particles. Sputtered material is then traced inside the simulation volume with initial angle and energy taken from cosine and Thompson distribution, respectively. Test particle approximation is assumed for impurity migration. Both Fokker–Planck and collisions with neutrals are accounted for during test particle motion, considering for the latter a neutral pressure of 0.1 Pa. A single time step of one second is considered in this study, since multiple steps showed not to influence the results. More accurate investigation will be

needed when trying to make comparison with experimental data in future works.

The GyM chamber is made of AISI 304 L stainless steel, with an iron (Fe), chromium (Cr) and nickel (Ni) content of about 70%, 18% and 8%. For this first modelling activity, the presence of other elements in the wall composition was neglected and a whole Fe chamber was considered. To address the behaviour of other impurities, identical simulations with different wall materials were performed. In particular, we investigated the behaviour of copper (Cu), as a proxy of stainless steel alloying metals (with specific reference to Ni, whose PWI parameters for He plasma were not available in ERO2.0 database), carbon (C) and tungsten (W), two fusion-relevant elements with low and high atomic number, respectively. The choice of W is further justified by the possibility to position a W liner in GyM that mimics a full W environment, which would allow an experimental benchmark of ERO2.0 results.

For each material, four different bias voltages were applied on the chamber components that are eroded the most by the plasma, namely the two bases and the bushings. The negative potentials were imposed with respect to the GyM vacuum chamber, considered at zero reference potential. No bias was instead applied to the lateral wall. This allowed to investigate the effect of bias on impurity migration. In fact, due to their geometry, bases and bushings have magnetic field lines directly impinging on their surfaces. On the contrary, as will be discussed in the following, lateral wall is mostly eroded by neutral impurities sputtered from bases and bushings, which are not influenced by the sheath electric field and applied bias. The study at different bias potentials is also motivated by the frequent use of biased samples in LPDs, to increase the energy of particles impinging on exposed samples. The different bias voltages were selected to analyze erosion near and well above the sputtering threshold energy of the different materials interacting with a He plasma (around 20 eV for C, Fe and Cu, 105–110 eV for W [28]). Thus, a negative bias from 0 to 200 V was used (in the following, we will always refer to its absolute value for simplicity).

To evaluate the energy of the ions impinging on the wall, beside the bias, we took into account the correction for the sheath potential, which depends on the local plasma parameters. This description results in monoenergetic plasma ions for each cell of the wall mesh. Eroded particles, instead, are traced by the code along their whole trajectory and present a distribution of impinging energies, as will be shown in the following.

ERO2.0 simulations at different biases were performed at fixed plasma background. None of the SOLPS-ITER simulations, in fact, include the presence of a bias at the targets. As a first approximation, it is expected that the presence of the bias only influences the plasma profiles within the sheath, while SOLPS mesh extends up to the sheath entrance.

It should be stressed that ERO2.0 simulations were performed considering only He⁺ ions in the plasma, thus neglecting He²⁺. This choice is justified by the SOLPS-ITER results reported in figure 3, which show an almost five orders of magnitude lower density for He²⁺ compared to He⁺ one.

The global erosion rate in terms of atoms eroded per second, computed integrating the erosion from both plasma

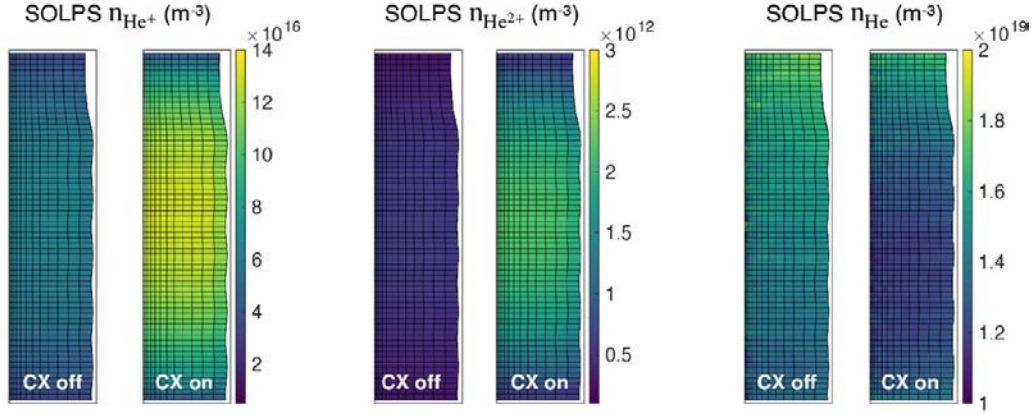


Figure 3. 2D density maps computed by SOLPS-ITER, without and with charge exchange (CX) reactions among ion (He^+ and He^{2+}) and neutral He populations.

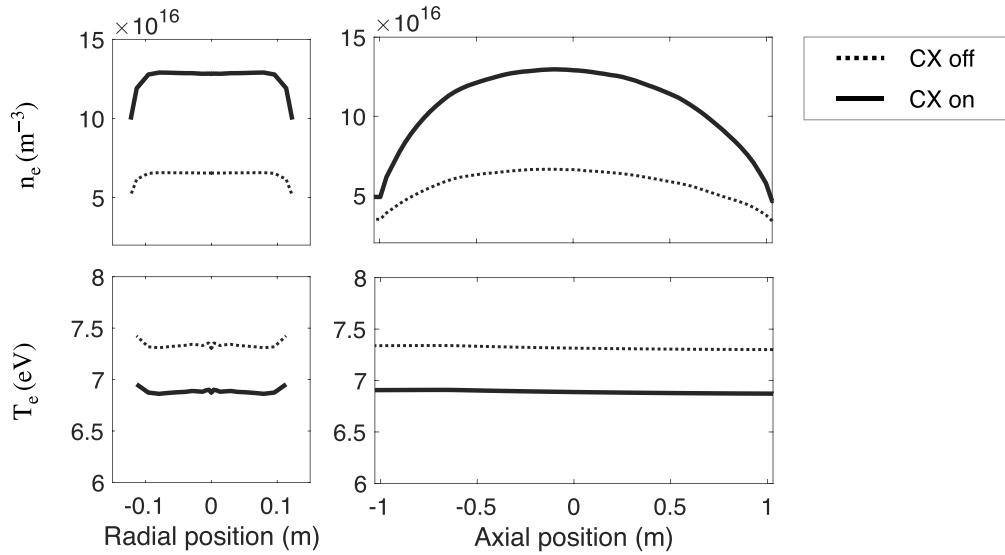


Figure 4. Radial (left) and axial (right) electron density and temperature profiles with and w/o CX reactions included in SOLPS-ITER simulations. The radial profiles are taken at $z=0$, i.e. at the axial centre of the plasma, and the axial profile is at $r=0$.

and traced particles over the whole modelled surfaces, is presented in figure 5, as a function of bias voltage and wall material. As expected, W is almost not eroded below 110 V for impinging He atoms and its erosion rate is at least one order of magnitude lower than that of the other elements. C, Fe and Cu show a similar behaviour especially at the higher biases, where Fe exhibits the highest erosion rate. By contrast, a few differences can be observed at the lower biases, due to the proximity to the sputtering threshold for those materials with He plasma.

We should also stress that these results were obtained considering the SOLPS-ITER plasma background with CX reactions on. As a comparison, ERO2.0 runs were also performed using the plasma background obtained turning off CX reactions. Peculiar effects were observed, in particular, when the ions energy at the wall is close to the sputtering threshold. Consider e.g. the case with Cu wall and biasing voltage 0 V and 100 V. According to Eckstein formulation [28], Cu sputtering threshold energy is around 20 eV, hence in the case with

no bias and giving $T_e \approx 7$ eV, ions acceleration due to sheath potential allows ions to reach the wall with an energy close to the sputtering threshold (always considering only He^+ ions). In the second case, instead, with $V_{\text{bias}} = 100$ V, ions energy is well above the sputtering threshold. The erosion rates corresponding to these two cases are shown with red stars in figure 5. Here, it can be seen that in the 0 V simulation the small increase of the average electron temperature (~ 0.5 eV) without CX reactions causes an increase of the erosion rate of more than one order of magnitude, despite the almost halving of the electron density (and subsequently of the ion flux). In fact, being in the proximity of the sputtering threshold means that small variations of ion impact energy can significantly influence the sputtering yield. On the contrary, sufficiently above the threshold as in the 100 V case, the sputtering yield is less sensitive to electron temperature and the reduction of the ion flux (caused by the lower electron density) results in a decrease of the global erosion.

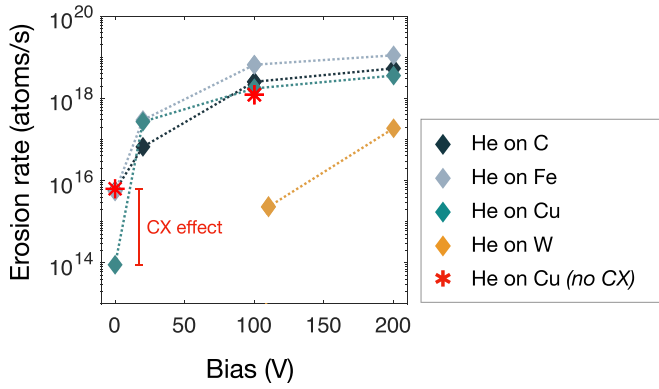


Figure 5. Global erosion rate, computed by ERO2.0 integrating the erosion over the whole modelled surfaces, as a function of the applied bias voltage. Different materials have been selected for the 3D wall elements from which erosion is computed.

3.3. Angular distribution of bushings erosion

Another important aspect that deserves a separate discussion is the erosion of bushings. As previously introduced, these small cylinders protrude radially into the 20 cm wide plasma for a length of about 2 cm. From the PWI point of view, their situation is particularly interesting. In fact, magnetic field lines impinge on bushings lateral wall, giving rise to a distribution of incident angles from grazing to orthogonal incidence. In a weak magnetic field, such as the one in GyM, where the ion Larmor radius ($\rho_i \approx 200 \mu\text{m}$) is of the same order of magnitude as the sheath thickness ($\lambda_s \approx 10\lambda_D \approx 700 \mu\text{m}$), ions are not completely forced to follow magnetic field lines and can be deflected by the sheath electric field.

In this first modelling attempt, we decided to investigate the two extreme cases for the plasma ions incidence angle θ in this situation: (a) θ equal to the angle between magnetic field lines and local surface normal or (b) $\theta = 0$ everywhere, namely complete deflection of plasma ions towards orthogonal incidence. In the real case, the situation would be somewhere in-between these extremes, according also to the bias voltage applied. However, a complete description of plasma ions trajectories in the sheath, e.g. using the sheath-tracing module implemented in ERO2.0, is out of the scope of this first modelling activity and could be investigated in future works (on the contrary, sheath deflection is always taken into account for test particles (TPs) eroded from walls).

The C, Fe, Cu and W erosion on bushings for case (i), as a function of local incidence angle and wall material, is depicted in figure 6(a), for the same He plasma background (CX on) and same bias voltage (200 V). Each point represents the erosion rate of a specific mesh cell on one of the GyM bushings, normalized to the maximum erosion rate on all bushings for each investigated material. The widening of the distributions at a fixed θ is due to the different axial locations of bushings: the ones closer to the bases are subjected to a lower particle flux due to a lower plasma density (see figure 3). Looking at figure 6(a), it is possible to observe the very peaked

distribution of W at orthogonal incidence, while both C and Cu present an erosion peak around 60° . On the other hand, Fe shows a less peaked distribution, with a maximum at around 30° which remains almost constant until 0° .

The same quantity for case (b), namely a fixed and orthogonal ion incidence angle, is reported in figure 6(b). In this situation, the assumption of complete deflection of plasma ions in the sheath results in the same angular distributions of normalized erosion for all materials, each one peaked at $\theta = 0$.

The reason behind this erosion behaviour can be ascribed to two competitive phenomena. On the one hand, the incoming ion flux reduces approaching grazing incidence due to simple geometrical reasons. On the other hand, sputtering yield increases at oblique angles, but its angular distribution depends on the sputtered material. This can be observed in figure 6(c), which shows the normalized sputtering yields of the different materials as a function of the ion incidence angle. The erosion observed in case (a) is the result of the competition between these two effects. In particular, the W sputtering yield presents a lower increase from orthogonal to grazing incidence, letting thus the reduction of flux prevail. The opposite occurs for C and Cu, where the higher yield at around 60° dominates on the reduction of the flux. The case of Fe is peculiar and the competition between the two phenomena leads to a distribution which is somehow in between the previous ones.

Considering now case (b), fixing the ion incidence angle in a normalized description of erosion with fixed bias voltage means inhibiting the variation of sputtering yield with angle, thus inhibiting also the main parameter dependent on the material in this framework. Therefore, it is not surprising that the angular distribution of erosion for this case reflects perfectly the reduction of the ion flux with angle, for all the different materials.

3.4. Impurities migration

After studying the erosion effects of the He plasma on the GyM wall, it is of interest to analyze the migration of eroded impurities, again as a function of material and bias voltage applied. As previously introduced, eroded impurities are modelled with ERO2.0 using the test particle approximation, namely they do not influence neither each other nor the plasma background. Therefore, we will not consider their effect on plasma parameters or the increased plasma cooling, which would need a further iterative SOLPS-ITER run. Moreover, TPs are launched according to the local erosion rate, which means that the large majority of TPs starts from the two bases of the GyM cylindrical chamber.

One of the most important parameters to understand migration behaviour is ionization fraction, defined as the number of ionization events divided by the total number of TPs. In other words, it may be interpreted as the average number of ionization events for each TP. Figure 7(a) shows the ionization fraction for each wall material, as a function of the bias voltage. Low bias values for W are not available, since W is

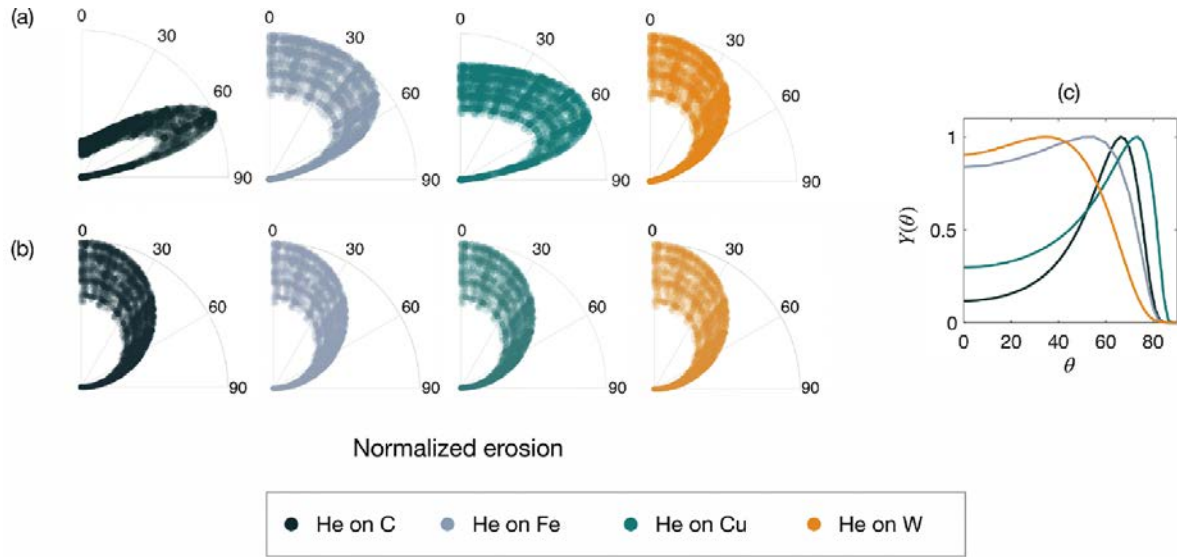


Figure 6. Polar plot of the angular distribution from 0° to 90° of the total erosion (normalized to the maximum for each material) computed by ERO2.0 onto the bushing elements, considering C, Fe, Cu and W as materials. (a) θ is the incidence angle between the magnetic field and the bushing surface element. (b) Sheath deflection is considered: ions reach the bushing surface element with orthogonal incidence. The angular distribution of the sputtering yield for the four different materials (normalized to the maximum for each material) is shown in (c).

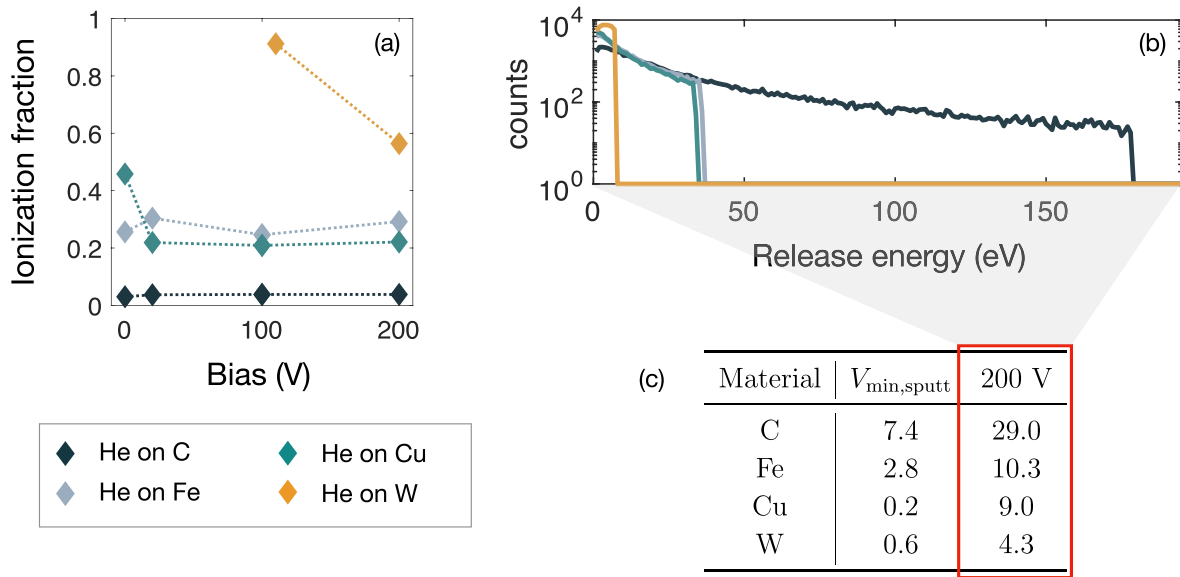


Figure 7. (a) Ionization fraction of eroded species, namely the number of ionization events divided by the total number of test particles, as a function of material and bias voltage. 0 and 20 V values for W are not available since no erosion could be observed in those cases. (b) Energy distribution of eroded particles at their release from the surface for the 200 V case. (c) Average value of the sputtered particles energy at their release from the surface (expressed in eV) at low ($V_{\min, \text{sputt}}$) and high voltage (200 V). $V_{\min, \text{sputt}}$ corresponds to the lowest bias above the sputtering threshold (110 V for W, 0 V for other materials).

not eroded in those conditions. The first comparison that can be made is between materials. C presents a consistently lower ionization (around 0.03) with respect to both Fe and Cu, which settle down in between 0.20 and 0.30. W shows the highest ionization fraction, always above 0.50. This behaviour can be immediately ascribed to the increase of the ionization probability with the atomic number Z of materials, and is in accordance with the ionization potentials reported in literature [29].

Another aspect that can be deduced from figure 7(a) is the dependence of ionization fraction on the bias voltage. In particular, for both Cu and W, a strong reduction of ionization is observed increasing the bias applied, while C and Fe show an almost constant behaviour. This result can be explained with the energy acquired by eroded species in different bias conditions, which has an influence on the interaction probability with plasma particles and, thus, on ionization.

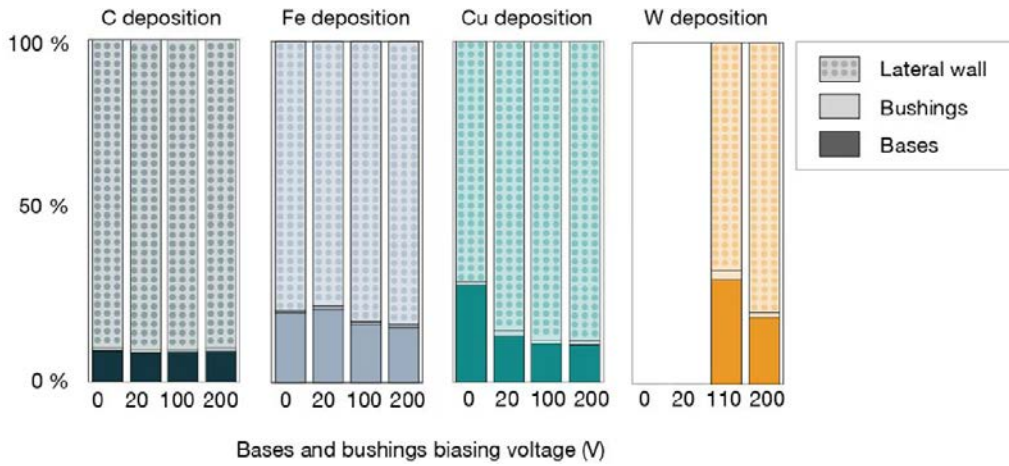


Figure 8. Deposition fraction of impurities on different 3D structures. Increasing bias is applied to the bases and to the bushings, but not to the lateral wall.

Figure 7(b) shows the energy spectra of sputtered particles for the 200 V case. Each material presents a distribution of release energies and, as expected, low Z material distributions extend up to higher energies, due to more efficient elastic collision energy transfer with He^+ ions. At lower voltages, when approaching the sputtering threshold, the energy distribution gets narrower and shifts towards lower energies. This can be observed in the table in figure 7(c), which shows the average release energy for each wall species at the lowest bias above sputtering threshold (110 V for W, 0 V for other materials) and in the 200 V case (which full energy distribution is shown in figure 7(b)). This observation is particularly evident for Cu and W, which present an extremely low average release energy (below 1 eV), mainly due to their higher Z . This extremely low release energy is, thus, the main cause of the observed increase in the ionization probability due to collisions with plasma particles.

Ionization has an important influence on TPs trajectories and on their redeposition location. In fact, only ions are bound to magnetic field lines, while neutrals simply escape. It should be pointed out that, in this work, no distinction is made between *prompt* and *global* redeposition. Thus, the two contributions to total deposition will be always presented together in the following. Figure 8 shows the deposition fraction of TPs, expressed in per cent, on the different parts of the GyM wall, namely the two bases of the cylinder, the lateral wall and the bushings, for all material and bias combinations. As could be expected, deposition is higher on the lateral wall, especially in the proximity of the two bases, which are the most eroded elements of the wall. Indeed, prompt redeposition on bases is less probable in a medium density plasma such as GyM one. Moreover, magnetic field lines impinge orthogonally on GyM bases, thus reducing the redeposition probability during the first gyro-orbit. However, the deposition fraction on bases varies significantly with material and is also higher at low bias for both Cu and W. This observation is in good agreement with the ionization behaviour described before. In fact, in GyM, magnetic field lines are almost axial

and directed towards the bases of the cylinder. Therefore, if the ionization fraction is high, more ions are produced and forced by the magnetic field to deviate from their trajectory and to redeposit on bases. A small percentage of ionized impurities, however, can still deposit on lateral wall thanks to cross-field transport.

Finally, it is important to analyse the impinging energy of TPs and their contribution to wall erosion, especially in high bias cases. Figure 9 reports the energy distribution of incident TPs with a bias of 200 V, as a function of wall material. The Fe distribution is equivalent to the Cu one, so it is not shown in figure. The presence of energy peaks confirms the observations on ionization made previously. In particular, W shows multiple peaks even at very high energy (around 700 eV), which is evidence of the presence of multiple ionized states. These peaks are well reduced for both Fe and Cu and are almost absent for C, in accordance with ionization results. TPs impinging with energy below 200 eV can be only neutrals or ions depositing on lateral wall, since bias is applied only on bases and bushings. Typical ion peaks, corresponding to multiples of the sheath potential, are clearly visible for W. C, instead, presents a prolonged distribution, with a shoulder at around 180 eV, which is in accordance with the energy acquired by C neutrals in a head-on collision with He (see figure 7(b)). Ion peaks in this low energy region are less visible for both Fe and Cu and the neutral energy distribution is reduced to lower energies with respect to C, as expected due to their higher Z .

The presence of high energy peaks for redepositing impurities could raise a few concerns related to wall erosion. Actually, considering the logarithmic scale in figure 9, higher ionization states are orders of magnitude less probable compared to lower ones. Moreover, the contribution of impurities to global erosion (integrated over all surfaces) is in the range 2%–4% for all the materials tested, while the remaining 95% is due to plasma erosion. However, this small percentage is not negligible especially for low- Z materials, since it is the only contribution to the erosion of GyM lateral wall, where magnetic field

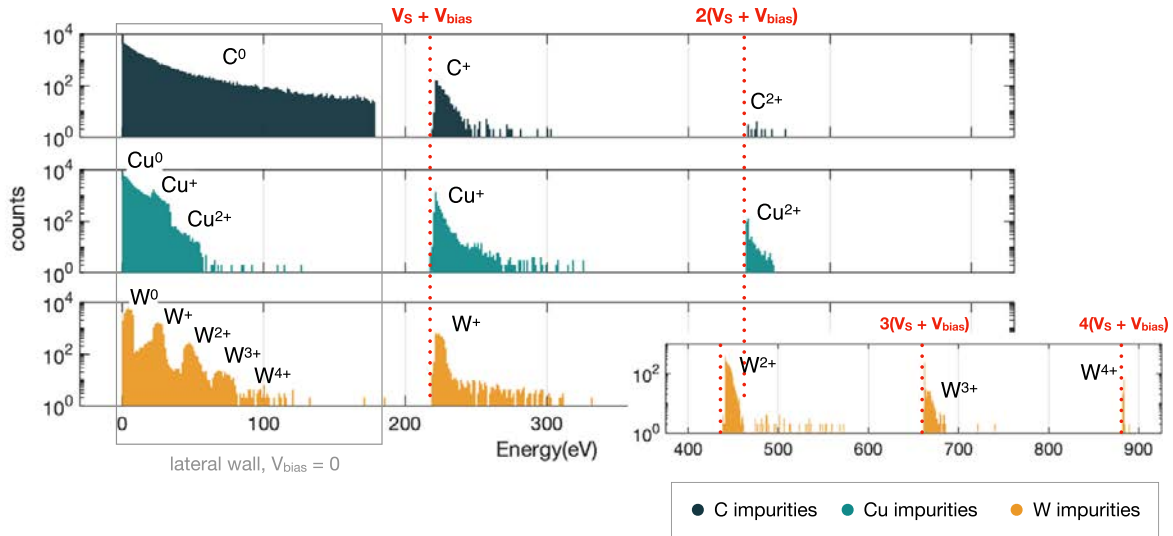


Figure 9. Energy distribution of depositing on the GyM wall. A biasing voltage $V_{\text{bias}} = 200$ V is applied to the bases and to the bushings. The Fe deposition distribution is equivalent to the Cu one, so it is not shown in figure.

lines are almost orthogonal to the surface normal and plasma erosion does not occur.

4. Conclusions

The study discussed in this paper presents the first global modelling of the PWI processes in the GyM linear device, obtained by coupling SOLPS-ITER and ERO2.0 codes. The simulations model in an integrated manner the plasma transport towards the PFCs, their erosion and the migration of the eroded impurities.

SOLPS-ITER simulations of pure He plasma in linear geometry were performed varying the database of atomic reactions between ions, electrons and neutral atoms. This work showed the importance of previously neglected reactions, such as charge exchange and radiative heat losses, and led to the modification of the default set of He reactions implemented in the code. The plasma background produced by SOLPS-ITER was then used in ERO2.0 simulations, highlighting the importance of an accurate estimation of plasma parameters, especially of the electron temperature, for an adequate evaluation of PWI phenomena. Even very small variations of the electron temperature, and hence of the sheath acceleration factor, were shown to be crucial near the sputtering threshold of the PFC materials. These results and the role of the newly introduced atomic reactions were demonstrated to be valid in temperature and densities regimes that are typical of a LPD. In light of the importance of He in ITER PFPO, it would be of great interest to generalize these studies also for typical tokamak edge plasma conditions.

Erosion of the GyM internal walls was investigated, varying wall material and bias voltage applied. The two bases of the GyM cylindrical chamber and the bushings were shown to be the main sources of impurities in the plasma. Erosion of bushings was studied considering two extreme assumptions,

namely no deflection of plasma ions in the sheath and complete deflection (orthogonal incidence). A more accurate modelling, e.g. using the sheath-tracing module implemented in ERO2.0, would be needed to reproduce the real situation occurring in GyM. It should be also pointed out that ideally flat surfaces have always been assumed in this work, while the presence of a micro-scale roughness would further increase the complexity.

Migration of eroded impurities in the whole volume of the device was also studied. The lateral wall was shown to be the sink for most of the redepositing particles. However, significant differences were observed changing wall material and bias voltage applied. The former result can be ascribed to the different ionization energy of the considered materials, which leads to a different probability of being axially confined by magnetic field lines. The latter, instead, can be related to the different energy acquired by sputtered particles, which is connected again to the ionization probability. As a future improvement, the modelling of the plasma background could self-consistently include impurities, by treating these species via the SOLPS-ITER multi-fluid model. This would allow to evaluate the effect of impurities on the plasma background, which is not considered by ERO2.0. Moreover, the modelling of impurity migration by ERO2.0, especially in machines with higher neutral density gradients than GyM, could benefit of the possibility of importing the full spatial distribution of neutrals from SOLPS-ITER.

To conclude, the results reported in this paper are the first step towards an integrated modelling of a realistic PWI experiment performed in GyM. To improve the present description, the simulation geometry should be modified to include the sample holder and its manipulator within the plasma volume. To do so, the recently developed extended grid in SOLPS-ITER [30] will be applied. Moreover, the benchmark of the obtained results against experimental data will be part of future studies.

Acknowledgment

The authors would like to acknowledge Detlev Reiter for the fruitful discussion and the help in implementing the new He atomic reactions in EIRENE input file.

G. Alberti acknowledges funding from Eni SpA for the PhD program.

This work has been carried out within the framework of the EUROfusion Consortium, funded by the European Union via the Euratom Research and Training Programme (Grant Agreement No 10 105 2200–EUROfusion). Views and opinions expressed are however those of the author(s) only and do not necessarily reflect those of the European Union or the European Commission. Neither the European Union nor the European Commission can be held responsible for them.

The views and opinions expressed herein do not necessarily reflect those of the ITER Organization.

ORCID iDs

G. Alberti  <https://orcid.org/0000-0001-9835-5085>
 E. Tonello  <https://orcid.org/0000-0001-8335-8873>
 A. Uccello  <https://orcid.org/0000-0003-3044-1715>
 J. Romazanov  <https://orcid.org/0000-0001-9439-786X>
 S. Brezinsek  <https://orcid.org/0000-0002-7213-3326>
 M. Passoni  <https://orcid.org/0000-0002-7844-3691>

References

- [1] Brezinsek S. et al 2017 *Nucl. Fusion* **57** 116041
- [2] Stangeby P. 2000 *The Plasma Boundary of Magnetic Fusion Devices (Series in Plasma Physics and Fluid Dynamics)* (Philadelphia, PA: Institute of Physics Publishing)
- [3] ITER Organization 2018 *Iter Research Plan Within the Staged Approach (Level III–Provisional Version)* (ITER Organization) p ITR-18-003
- [4] Hakola A. et al 2021 *Nucl. Fusion* **61** 116006
- [5] Tsitrone E. et al 2021 *Nucl. Fusion* **62** 076028
- [6] Brezinsek S. 2022 Gross erosion of tungsten in hydrogen, deuterium, tritium plasmas in JET equipped with beryllium first wall and tungsten divertor *25th Int. Conf. on Plasma Surface Interaction in Controlled Fusion Devices (13–17 June)* (available at: www.psi2022.kr/)
- [7] Ohno N. et al 2019 *Nucl. Mater. Energy* **19** 458–62
- [8] Tanaka H., Hayashi Y., Kajita S., van der Meiden H. J., Yoshikawa M., Vernimmen J. W. M., Scholten J., Classen I., Morgan T. W. and Ohno N. 2020 *Plasma Phys. Control. Fusion* **62** 115021
- [9] Baldwin M. and Doerner R. 2008 *Nucl. Fusion* **48** 035001
- [10] Kajita S., Sakaguchi W., Ohno N., Yoshida N. and Saeki T. 2009 *Nucl. Fusion* **49** 095005
- [11] Sakamoto R., Bernard E., Kreter A. and Yoshida N. 2016 *Nucl. Fusion* **57** 016040
- [12] Wiesen S. et al 2015 *J. Nucl. Mater.* **463** 480–4
- [13] Bonnin X. et al 2016 *Plasma Fusion Res.* **11** 1403102
- [14] Romazanov J. et al 2017 *Phys. Scr.* **T170** 014018
- [15] Baeva M., Goedheer W., Cardozo N.L. and Reiter D. 2007 *J. Nucl. Mater.* **363–365** 330–4
- [16] Owen L.W., Caneses J.F., Canik J., Lore J.D., Corr C., Blackwell B., Bonnin X. and Rapp J. 2017 *Plasma Sources Sci. Technol.* **26** 055005
- [17] Kaffle N., Owen L. W., Caneses J. F., Biewer T. M., Caughman J. B. O., Donovan D. C., Goulding R. H. and Rapp J. 2018 *Phys. Plasmas* **25** 052508
- [18] Eksaeva A. et al 2020 *Phys. Scr.* **T171** 014057
- [19] Uccello A. et al 2020 *Nucl. Mater. Energy* **25** 100808
- [20] Sala M., Tonello E., Uccello A., Bonnin X., Ricci D., Dellasega D., Granucci G. and Passoni M. 2020 *Plasma Phys. Control. Fusion* **62** 055005
- [21] Tonello E., Formenti A., Alberti G., Uccello A. and Passoni M. 2021 *Nucl. Fusion* **61** 066036
- [22] Alberti G., Sala M., Romazanov J., Uccello A., Dellasega D. and Passoni M. 2021 *Nucl. Fusion* **61** 066039
- [23] Romazanov J. et al 2019 *Nucl. Mater. Energy* **18** 331–8
- [24] Genova S.D. et al 2021 *Nucl. Fusion* **61** 106019
- [25] Romazanov J. et al 2022 *Nucl. Fusion* **62** 036011
- [26] Rozhansky V. et al 2009 *Nucl. Fusion* **49** 025007
- [27] Summers H.P., Dickson W.J., O'Mullane M.G., Badnell N.R., Whiteford A.D., Brooks D.H., Lang J., Loch S.D. and Griffin D.C. 2006 *Plasma Phys. Control. Fusion* **48** 263–93
- [28] Eckstein W., Garcia-Rosales C., Roth J. and Ottenberger W. 1993 *Sputtering Data* (Garching, DE: Max-Planck-Institut für Plasmaphysik)
- [29] Kramida A., Ralchenko Y., Reader J. and NIST ASD Team 2021 *NIST Atomic Spectra Database (ver. 5.9)* (Gaithersburg, MD: National Institute of Standards and Technology) (available at: <https://physics.nist.gov/asd>) (Accessed 2 May 2022)
- [30] Dekeyser W. et al 2021 *Nucl. Mater. Energy* **27** 100999